

Article

Magnetocaloric Properties of Melt-Extracted Gd-Co-Al Amorphous/Crystalline Composite Fiber

Fan Chen ^{1,2}, Kun Han ², Meng Gao ², Yan Zhang ², Wei Xu ², Juntao Huo ^{2,*}, Changjiang Zhang ^{1,*}, Lijian Song ^{2,*} and Jun-Qiang Wang ^{2,*}

¹ School of Materials Science and Engineering, Taiyuan University of Technology, Taiyuan 030024, China

² CAS Key Laboratory of Magnetic Materials and Devices, and Zhejiang Province Key Laboratory of Magnetic Materials and Application Technology, Ningbo Institute of Materials Technology and Engineering, Chinese Academy of Sciences, Ningbo 315201, China

* Correspondence: huojuntao@nimte.ac.cn (J.H.); zcj0408@163.com (C.Z.); songlj@nimte.ac.cn (L.S.); jqwang@nimte.ac.cn (J.-Q.W.)

Abstract: In this work, a series of Gd-based amorphous/crystalline composite fibers (ANCFs) were prepared by regulating the Gd content in Gd-Co-Al alloys using the melt-extracted method. Compared to the amorphous alloy, the ANCFs display excellent magnetic refrigeration capacity (*RC*). Among them, Gd₈₅Co₅Al₁₀ ANCF had the largest *RC* (841 J kg⁻¹) and the widest working temperature range (245 K). Compared with Gd₇₀Co₁₀Al₂₀, *RC* and working temperature range increased by 56% and 119%, respectively. This superior property is attributed to the ideal coupling between the amorphous phase and the crystalline. This result opens a new door to optimize the magnetic refrigeration capacity by controlling the amorphous crystalline composite structure.

Keywords: magnetocaloric effect; magnetic refrigeration; Gd-based composites; composite fibers



Citation: Chen, F.; Han, K.; Gao, M.; Zhang, Y.; Xu, W.; Huo, J.; Zhang, C.; Song, L.; Wang, J.-Q. Magnetocaloric Properties of Melt-Extracted Gd-Co-Al Amorphous/Crystalline Composite Fiber. *Metals* **2022**, *12*, 1367. <https://doi.org/10.3390/met12081367>

Academic Editor: Volodymyr A. Chernenko

Received: 12 July 2022

Accepted: 10 August 2022

Published: 18 August 2022

Publisher's Note: MDPI stays neutral with regard to jurisdictional claims in published maps and institutional affiliations.



Copyright: © 2022 by the authors. Licensee MDPI, Basel, Switzerland. This article is an open access article distributed under the terms and conditions of the Creative Commons Attribution (CC BY) license (<https://creativecommons.org/licenses/by/4.0/>).

1. Introduction

Unlike the conventional gas-compression refrigeration, magnetic refrigeration has attracted much attention for being an ideal candidate in refrigeration because of its advantages in environmental friendliness and energy efficiency [1–4]. Magnetocaloric effect (MCE) is a thermal response caused by the change of magnetic entropy for a varying magnetic field. Magnetocaloric materials with specific magnetocaloric properties are the core issue for their actual applications, e.g., adjustable magnetic transition temperature (T_C), large magnetic entropy change ($-\Delta S_M$), large *RC*, and wide working temperature range [5,6]. Previous works show that the rare earth (RE)-based alloys usually perform better in MCE than transition metals such as Fe- or Mn-based alloys [1–3,5,7–19]. For example, RE-based amorphous alloys show reduced Curie temperature (T_C), a wider working temperature range, and higher *RC* [20], which bestows them with superior potential refrigerants for cryogenic refrigeration, such as at liquid nitrogen temperatures or liquid helium temperatures [6,21]. However, the reduced T_C limits their refrigeration ability near room temperature [15,20,22,23].

To enhance the temperature range of magnetocaloric materials, the other phases with different T_C were induced [6,24–26]. For example, the composite of Gd₆₅Mn₂₅Si₁₀ amorphous ribbons and Gd sheets induced by hot-pressing displays a table-like magnetic entropy change in a wide temperature range 73 K [25]. However, without metallurgical grade bonding, composites prepared by physical compounding methods like hot-pressing have weakened strength and thermal conductivity. On the other hand, the amorphous/crystalline composites can also be achieved by the composition design or a part-crystallization annealing for amorphous alloys [6,21,26]. In these processes, the metallurgical grade-binding between different phases can be achieved, which promotes the refrigeration abilities of samples. Besides, the melt extraction method with high heat

transfer capacity was used to prepare the fibers, which have relatively high magnetic, thermal, electrical and mechanical properties [6,27–29].

In this work, a series of Gd-Co-Al amorphous/nanocrystalline composites fibers (ANCFs) have been prepared by the melt-extraction method. The optimal refrigeration ability was determined by the wide working temperature range from 50 K to 295 K, large $-\Delta S_M$ ($8.7 \text{ J kg}^{-1} \text{ K}^{-1}$) and RC (841 J kg^{-1}) when the Gd content is at 85%. Besides, the optimal refrigeration ability of $\text{Gd}_{85}\text{Co}_5\text{Al}_{10}$ originates from the coupling effect between crystalline Gd and an amorphous matrix. This result suggests that the amorphous/crystalline composite formed by composition design has potential to be a new method to fabricate superior magnetocaloric materials.

2. Experimental Details

The master alloys with nominal composition of $\text{Gd}_{70}\text{Co}_{10}\text{Al}_{20}$, $\text{Gd}_{80}\text{Co}_{10}\text{Al}_{10}$, $\text{Gd}_{85}\text{Co}_5\text{Al}_{10}$, and $\text{Gd}_{80}\text{Co}_5\text{Al}_{15}$ (at.%) were fabricated by arc melting pure Gd, Co and Al in a Ti-gettered argon atmosphere. In addition, the master alloys were prepared for micron fibers by the melt-extraction method (10 m/s). The phase compositions were examined by X-ray diffraction (XRD, Bruker D8 Advance) with Cu $K\alpha$ radiation, and the specimen was scanned over a 2θ range from 20° to 90° at $6^\circ/\text{min}$. The surface and cross-section of the fibers were observed by scanning electron microscopy (SEM, EVO18, ZEISS, Berlin, Germany) at operating voltages of 20 kV. The microstructures were examined by transmission electron microscopy (TEM, Thermo Fisher, Talos F200 \times , Waltham, MA, USA) at operating voltages of 200 kV, bright field image (BF) and selected-area electron diffraction (SAED) of the different electron beam incident axis were used to investigate the microstructure of the ANCF specimen. The magnetic properties were then measured using the Magnetic Property Measurement System (MPMS, Quantum Design Int., San Diego, CA, USA).

3. Results and Discussion

In Figure 1a, the schematic melt-extraction method for preparing Gd-Co-Al fibers is given. The master alloy ingot was melted in a high-frequency-induced current, and the high-speed rotation Mo wheel spun out the melt and formed the fibers finally. The length of prepared fibers was about 15 cm, as shown in Figure 1b. SEM results show that the prepared fibers exhibit narrow distribution of size, and that their diameter is about $70 \mu\text{m}$ for the $\text{Gd}_{85}\text{Co}_5\text{Al}_{10}$ sample. Besides, the fibers were not cylindrical in a regular manner because of the surface tension during the melt-extraction process, as shown in Figure 1c–e. Notably, fibers have better application performance compared with their bulk or ribbon counterparts because their large surface area enhances the heat-exchange efficiency [27–29].

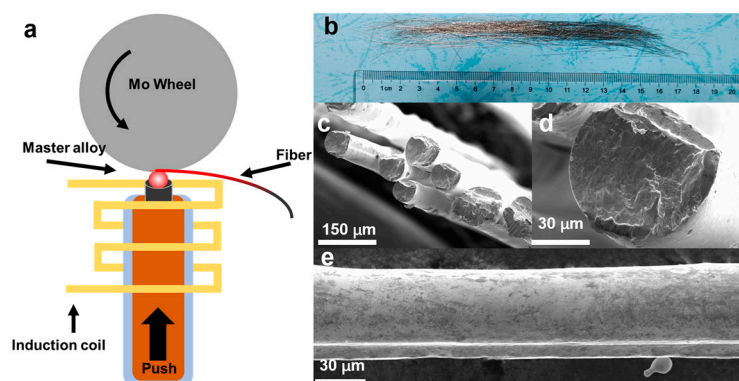


Figure 1. (a) The diagram of melt-extraction method, (b) the image, and (c–e) the SEM images of $\text{Gd}_{85}\text{Co}_5\text{Al}_{10}$ ANCF.

The XRD patterns of the $\text{Gd}_{70}\text{Co}_{10}\text{Al}_{20}$, $\text{Gd}_{80}\text{Co}_{10}\text{Al}_{10}$, $\text{Gd}_{80}\text{Co}_5\text{Al}_{15}$ and $\text{Gd}_{85}\text{Co}_5\text{Al}_{10}$ as-cast fibers is shown in Figure 2. For $\text{Gd}_{70}\text{Co}_{10}\text{Al}_{20}$, the XRD pattern only shows a broad hump, which indicates its pure amorphous structure. For $\text{Gd}_{80}\text{Co}_{10}\text{Al}_{10}$, $\text{Gd}_{80}\text{Co}_5\text{Al}_{15}$,

and $\text{Gd}_{85}\text{Co}_5\text{Al}_{10}$, crystal peaks appear in their XRD patterns, which were contributed by Gd crystal. It is interesting that the $(10\bar{1}3)$ peak of Gd appears in the XRD pattern for $\text{Gd}_{85}\text{Co}_5\text{Al}_{10}$, besides the (0002) , $(10\bar{1}0)$ and $(20\bar{2}2)$ peaks. The above results indicate that high Gd content reduces glass-forming abilities and favors the formation of Gd crystal. In other words, the phase compositions of Gd-Co-Al alloys can be adjusted by regulating the Gd content.

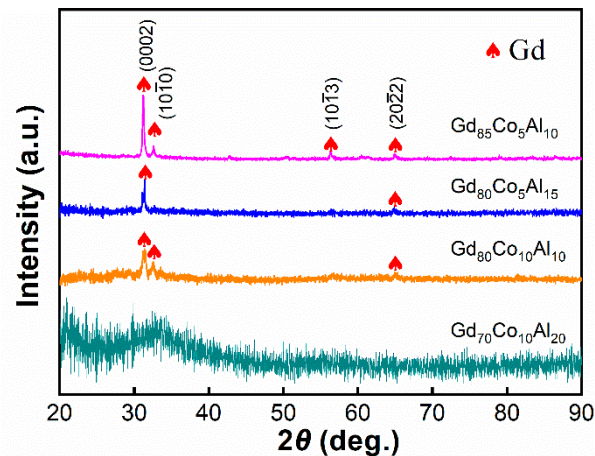


Figure 2. XRD patterns of Gd-Co-Al metal fibers.

The microstructures of $\text{Gd}_{85}\text{Co}_5\text{Al}_{10}$ were further identified by TEM and EDS (Energy Dispersive Spectroscopy) mapping. The results have shown in Figure 3a–d. As shown in Figure 3a, $\text{Gd}_{85}\text{Co}_5\text{Al}_{10}$ has amorphous/crystalline composite structures, in which the island-like crystal phase is embedded in the river-like amorphous matrix. The size of the crystal phase is 300~500 nm. In Figure 3b, the high-resolution TEM (HRTEM) shows the amorphous maze-like pattern and crystal lattice fringes pattern in regions A and B, respectively. Moreover, Figure 3c shows the selected-area electron diffraction (SAED) for region A, which confirmed its pure amorphous structures. Additionally, in Figure 3d, the SAED for region B is confirmed as the hexagonal Gd $(10\bar{1}0)$ zonal axis. The EDS-mapping result further suggests that the nanocrystals were in the Gd phase, as shown in Figure 3e. Based on the above results, we confirmed the nature of ANCF for the $\text{Gd}_{85}\text{Co}_5\text{Al}_{10}$ sample. This conclusion is also applicable to $\text{Gd}_{80}\text{Co}_{10}\text{Al}_{10}$ and $\text{Gd}_{80}\text{Co}_5\text{Al}_{15}$ samples.

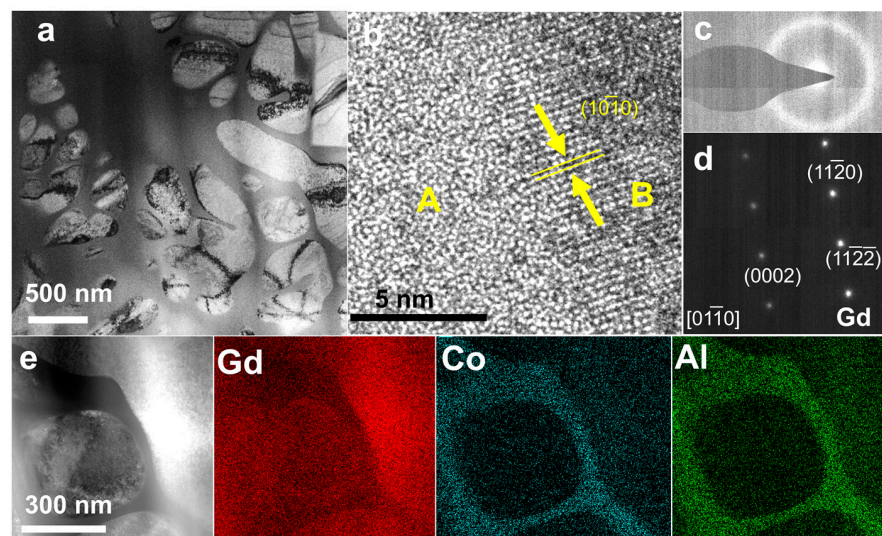


Figure 3. (a) The morphology of $\text{Gd}_{85}\text{Co}_5\text{Al}_{10}$, (b) HRTEM of $\text{Gd}_{85}\text{Co}_5\text{Al}_{10}$, (c) SAED of the amorphous part of $\text{Gd}_{85}\text{Co}_5\text{Al}_{10}$, (d) SAED of the crystalline part of $\text{Gd}_{85}\text{Co}_5\text{Al}_{10}$, (e) the Gd, Co, Al are the EDS-mapping results.

For these samples, the temperature dependences of magnetic behavior were measured under a 200 Oe magnetic field. As shown in Figure 4a–d, the zero-field cooling (ZFC) curves and field-cooling (FC) curves separate at about 50 K, which means that the spin freezing temperatures for all samples is about 50 K [30]. For $\text{Gd}_{70}\text{Co}_{10}\text{Al}_{20}$, there is only one T_C at 101 K, as shown in the insert of Figure 4a. For ANCFs there were two magnetic transition temperatures belonging to the amorphous and crystalline phases separately, as shown in Figure 4c,d. The T_{C1} of the amorphous phase were 116, 98, 98 K, and the T_{C2} of the crystalline phases were 271, 264, 264 K for $\text{Gd}_{80}\text{Co}_5\text{Al}_{15}$, $\text{Gd}_{80}\text{Co}_{10}\text{Al}_{10}$ and $\text{Gd}_{85}\text{Co}_5\text{Al}_{10}$ ANCFs, respectively. These results are also listed in Table 1.

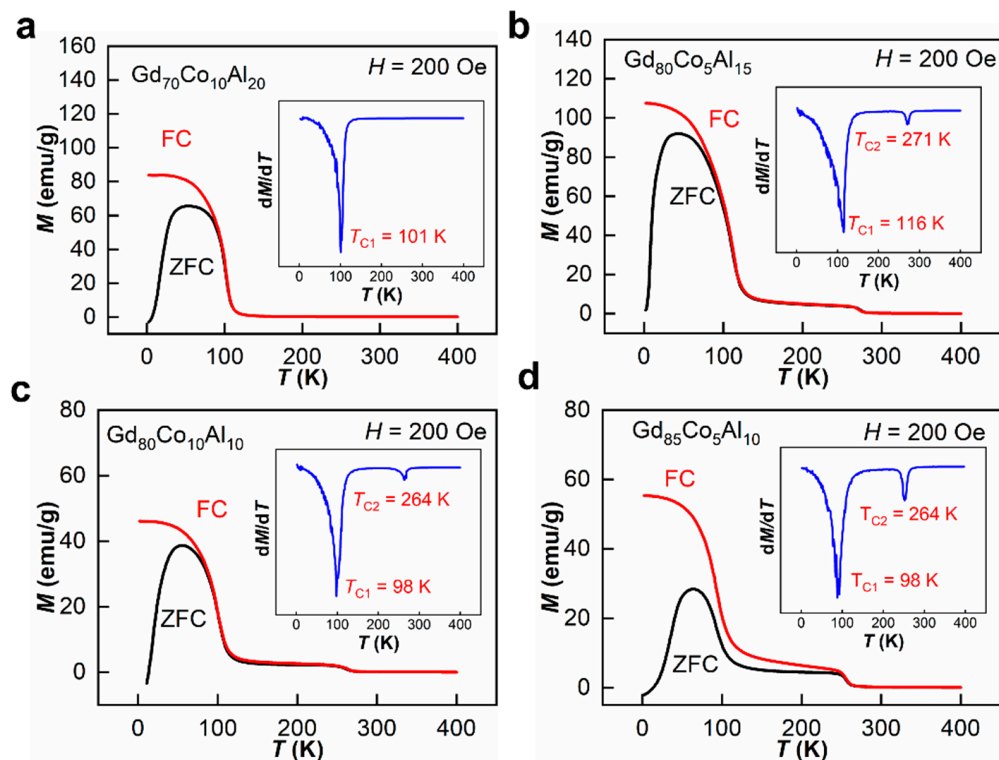


Figure 4. Temperature dependences of zero field cooling (ZFC) and field cooling (FC) magnetization under a magnetic field of 200 Oe, (a) $\text{Gd}_{70}\text{Co}_{10}\text{Al}_{20}$, (b) $\text{Gd}_{80}\text{Co}_5\text{Al}_{15}$, (c) $\text{Gd}_{80}\text{Co}_{10}\text{Al}_{10}$, (d) $\text{Gd}_{85}\text{Co}_5\text{Al}_{10}$. The insets are dM/dT curves of FC, respectively.

Table 1. The magnetic transition temperature (T_{tran}), peak value of magnetic entropy change ($-\Delta S_M^{\text{pk}}$), full width at half-maximum of $-\Delta S_M$ peak (ΔT_{FWHM}), refrigeration capacity (RC) under a maximum applied field of 5 T for some selected Gd-based magnetic refrigeration material.

No.	Composition	T_{tran} (K)	$-\Delta S_M^{\text{pk}}$ ($\text{J kg}^{-1} \text{K}^{-1}$)	ΔT_{FWHM} (K)	RC (J kg^{-1})	Ref.
1	$\text{Gd}_{70}\text{Co}_{10}\text{Al}_{20}$	101	6.36	112	538	This work
2	$\text{Gd}_{80}\text{Co}_5\text{Al}_{15}$	116/271	4.06/2.64	220	622	This work
3	$\text{Gd}_{80}\text{Co}_{10}\text{Al}_{10}$	98/264	4.31/3.29	207	625	This work
4	$\text{Gd}_{85}\text{Co}_5\text{Al}_{10}$	98/264	4.24/5.07	245	841	This work
5	Gd_4Co_3	208	7.2	~	547	[31]
6	$\text{Gd}_{55}\text{Al}_{25}\text{Co}_{20}$	100	9.7	~	652	[15]
7	$\text{Gd}_{50}\text{Co}_{45}\text{Fe}_5$	289	3.8	~	521	[12]
8	$\text{Gd}_{53}\text{Al}_{24}\text{Co}_{20}\text{Zr}_3$	93	9.4	~	590	[13]
9	$\text{Gd}_5\text{Si}_2\text{Ge}_2$	276	18.6	~	306	[32]
10	Gd	294	10.2	~	410	[33]

The magnetocaloric properties were investigated by measuring the isothermal magnetization curves for these fibers. In Figure 5a,b, the M - H curves and Arrot plot for $\text{Gd}_{85}\text{Co}_5\text{Al}_{15}$ ANCF are given. In Figure 5a, magnetization continually changes following

the changes of an applied magnetic field; thus there were no features of field-induced phase transition, which is the characteristic of first-order magnetic transition [28,34]. In Figure 5b, the positive slopes further confirmed the second-order magnetic phase transition of both the amorphous and crystalline phases for ANCFs [35]. The second-order magnetic transition had almost zero magnetic and thermal hysteresis, benefiting from a wide working temperature range [34,36]. These features ensure the magnetocaloric performances for ANCFs.

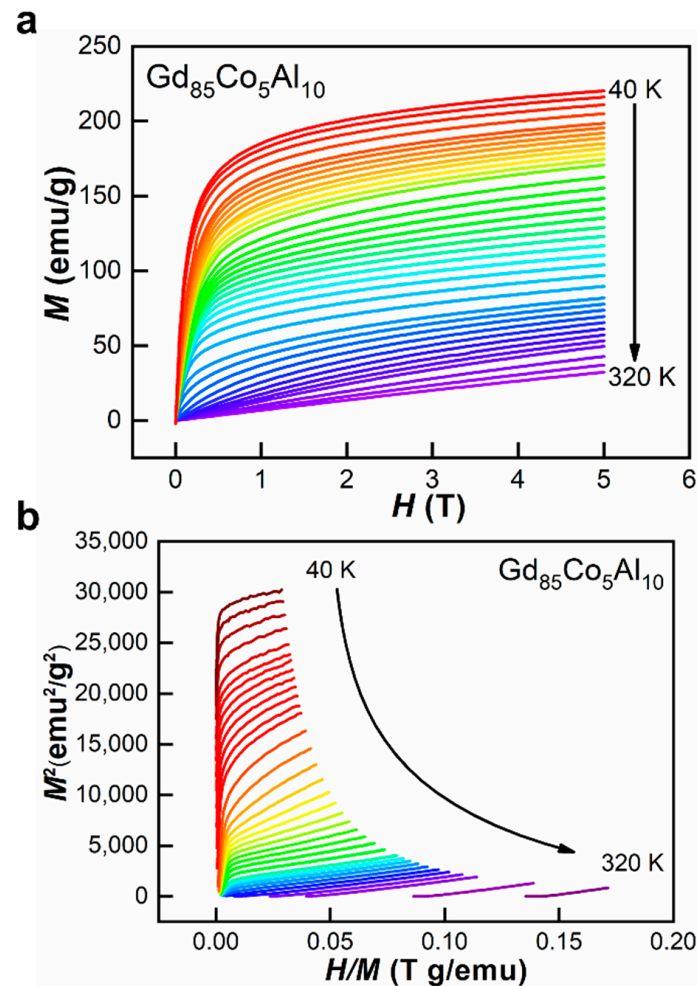


Figure 5. (a) Isothermal magnetization curves and (b) Arrott plots of $Gd_{85}Co_5Al_{10}$ ANCF.

The ΔS_M in the different applied magnetic fields can be calculated using the following equation [37]:

$$\Delta S_M(T, H) = \frac{\int_0^H M(T_i, H) dH - \int_0^H M(T_{i+1}, H) dH}{T_i - T_{i+1}} \quad (1)$$

Figure 6a–d show the temperature dependences of $-\Delta S_M$ in the different magnetic fields. In Figure 6a, for $Gd_{70}Co_{10}Al_{20}$, there is only one $-\Delta S_M$ peak around 100 K due to its pure amorphous structures, and the peak value is $6.36 \text{ J kg}^{-1} \text{ K}^{-1}$ ($H = 5 \text{ T}$). For ANCFs, two $-\Delta S_M$ peaks belong to the amorphous and crystalline phases, respectively. With the increase of Gd content, the peak values of $-\Delta S_M$ near 100 K decreases gradually. Meanwhile, the peak values of $-\Delta S_M$ around 270 K were strengthened with the increase of the crystalline Gd phase. At $H = 5 \text{ T}$, the first $-\Delta S_M$ peak values were $4.31 \text{ J kg}^{-1} \text{ K}^{-1}$, $4.06 \text{ J kg}^{-1} \text{ K}^{-1}$ and $4.24 \text{ J kg}^{-1} \text{ K}^{-1}$, and at the second $-\Delta S_M$ peak values were $3.29 \text{ J kg}^{-1} \text{ K}^{-1}$, $2.64 \text{ J kg}^{-1} \text{ K}^{-1}$ and $5.07 \text{ J kg}^{-1} \text{ K}^{-1}$ for $Gd_{80}Co_{10}Al_{10}$, $Gd_{80}Co_5Al_{15}$ and $Gd_{85}Co_5Al_{10}$ ANCFs, respectively. These values are listed in Table 1. The above results show that the amount of Gd crystalline phases of ANCFs can enhance the RC near room temperature.

Especially, $\text{Gd}_{85}\text{Co}_5\text{Al}_{10}$ ANCF not only had the highest $-\Delta S_M$ peak value but also the crystalline phase had a similar $-\Delta S_M$ peak value to that of the amorphous phase, thus the ratio of amorphous and crystalline phases is optimal in $\text{Gd}_{85}\text{Co}_5\text{Al}_{10}$ ANCF. Because of this optimal ratio, $\text{Gd}_{85}\text{Co}_5\text{Al}_{10}$ ANCF keeps a large magnetic entropy change in 50~300 K, thus $\text{Gd}_{85}\text{Co}_5\text{Al}_{10}$ ANCF is promising for a large application temperature span. Although the $-\Delta S_M$ peak values decreased due to the composite structure for ANCF, it is worth noting that such values were still larger than those of transition metals [38–42].

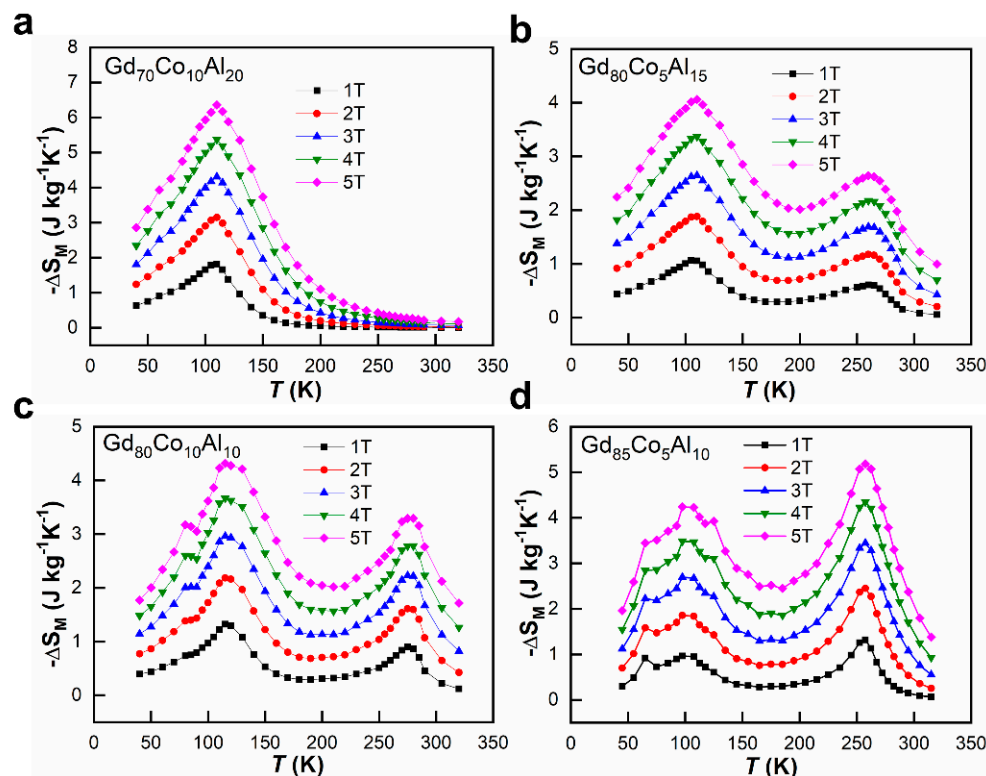


Figure 6. $-\Delta S_M$ as a function of temperature under the magnetic fields of 1, 2, 3, 4 and 5 T for (a) $\text{Gd}_{70}\text{Co}_{10}\text{Al}_{20}$; (b) $\text{Gd}_{80}\text{Co}_5\text{Al}_{15}$; (c) $\text{Gd}_{80}\text{Co}_{10}\text{Al}_{10}$; (d) $\text{Gd}_{85}\text{Co}_5\text{Al}_{10}$.

RC is an important parameter indicating the efficiency of magnetic refrigerant. Here RC is obtained by using the following equation:

$$RC = \int_{T_1}^{T_2} \Delta S_M(T) dT \quad (2)$$

where T_1 and T_2 are identified by the temperature values at half height of magnetic entropy change peaks. For amorphous $\text{Gd}_{70}\text{Co}_{10}\text{Al}_{20}$, the RC is 538 J kg^{-1} . For $\text{Gd}_{80}\text{Co}_{10}\text{Al}_{10}$, $\text{Gd}_{80}\text{Co}_5\text{Al}_{15}$ and $\text{Gd}_{85}\text{Co}_5\text{Al}_{10}$ ANCF, the RCs were 622 J kg^{-1} , 625 J kg^{-1} , and 841 J kg^{-1} , respectively. Compared to $\text{Gd}_{70}\text{Co}_{10}\text{Al}_{20}$, the RC of ANCF is significantly improved due to the formation of crystalline Gd. $\text{Gd}_{85}\text{Co}_5\text{Al}_{10}$ ANCF shows the best performance, which is an increase of about 56% compared to pure amorphous $\text{Gd}_{70}\text{Co}_{10}\text{Al}_{20}$. Just as important, the range of working temperature range for $\text{Gd}_{85}\text{Co}_5\text{Al}_{10}$ can be as wide as 245 K from room temperature to liquid nitrogen temperature, which was also the best performance and was about 119% higher than $\text{Gd}_{70}\text{Co}_{10}\text{Al}_{20}$. Such a performance also proved the optimal ratio of amorphous and crystalline phases in $\text{Gd}_{85}\text{Co}_5\text{Al}_{10}$ ANCF.

To further distinguish the contributions from both phases in ANCF, the $-\Delta S_M$ - T curves were fitted by the Gaussian peak function. The reliability of the fitting results was confirmed by the coefficient of determination R^2 (≥ 0.917). In Figure 7a, there is only one fitted peak belonging to the amorphous phase of $\text{Gd}_{70}\text{Co}_{10}\text{Al}_{20}$. For ANCF, the contribution from the amorphous phase decreased with increasing Gd content, while the contribution

from the crystalline phase increased, as shown in Figure 7b–d. In the $\text{Gd}_{85}\text{Co}_5\text{Al}_{10}$ ANCF, amorphous and crystalline phases comparably contributed to magnetocaloric performance.

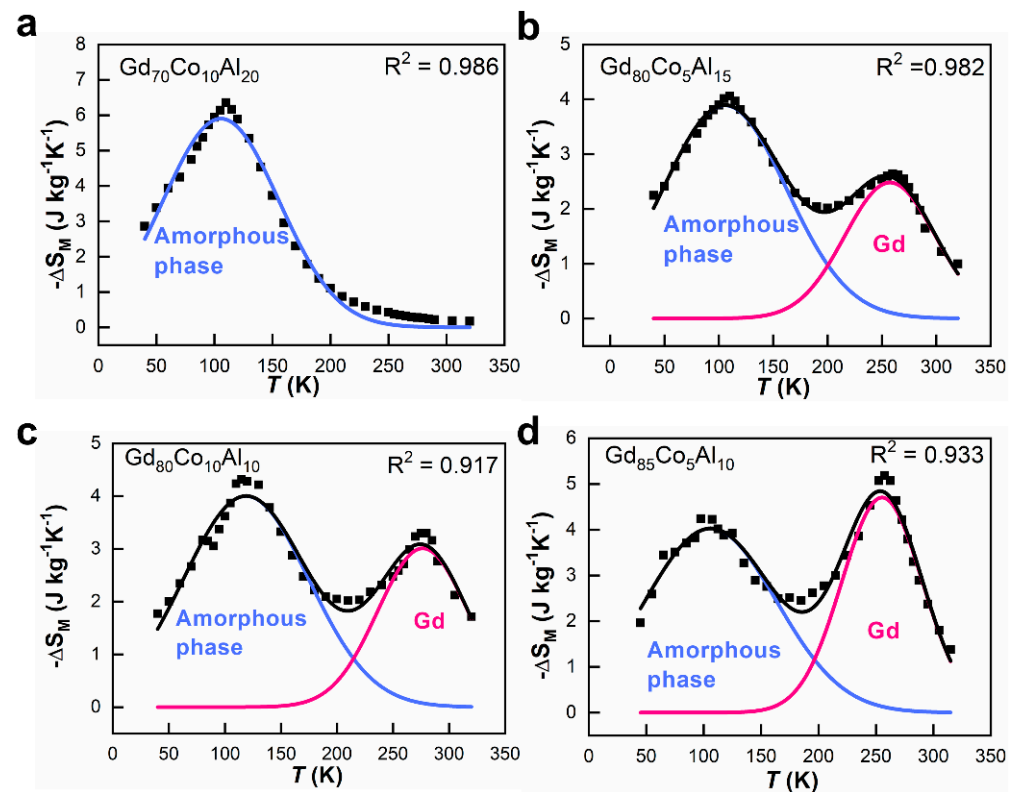


Figure 7. The fitting results of the contribution of both the amorphous phase (blue curve) and the crystalline phase (red curve) to the total $-\Delta S_M$ - T curve (solid square) of fibers under a field change of 5 T. (a) $\text{Gd}_{70}\text{Co}_{10}\text{Al}_{20}$; (b) $\text{Gd}_{80}\text{Co}_5\text{Al}_{15}$; (c) $\text{Gd}_{80}\text{Co}_{10}\text{Al}_{10}$; (d) $\text{Gd}_{85}\text{Co}_5\text{Al}_{10}$.

The fitted peak value of $-\Delta S_M$ and RC for both phases are shown in Figure 8a,b. The $-\Delta S_M$ and RC of $\text{Gd}_{70}\text{Co}_{10}\text{Al}_{20}$ were completely in the amorphous phase. It was obvious that with the increase of Gd content, the $-\Delta S_M^{\text{pk}}$ and RC of crystal Gd gradually increased, which further indicated the positive correlation between the Gd content in alloy and the crystal Gd content in ANCFs. Once the Gd crystalline phase appeared, the magnetic entropy changed peaks and RC was enhanced obviously, which reflected the coupling effect between the amorphous and Gd phase improved the refrigeration ability. For the best magnetocaloric performance of $\text{Gd}_{85}\text{Co}_5\text{Al}_{10}$ ANCF, the magnetic entropy change peaks were $4.0 \text{ J kg}^{-1} \text{ K}^{-1}$ and $4.7 \text{ J kg}^{-1} \text{ K}^{-1}$, and the RC values were $477 \text{ J kg}^{-1} \text{ K}^{-1}$ and $364 \text{ J kg}^{-1} \text{ K}^{-1}$ for amorphous and crystalline phases, respectively. In other words, the optimal ratio of amorphous and crystalline phases was established in $\text{Gd}_{85}\text{Co}_5\text{Al}_{10}$ ANCF.

To analyze the MCE performance characteristics of ANCFs, the RC and T_C of typical Gd-based comparisons are summarized in Figure 9, including Gd-based metallic glasses (MG), Gd-based crystals, and $\text{Gd}_{85}\text{Co}_5\text{Al}_{10}$. These results are also listed in Table 1. The $\text{Gd}_{85}\text{Co}_5\text{Al}_{10}$ ANCF possessed the largest RC of $841 \text{ J kg}^{-1} \text{ K}^{-1}$ and widest working temperature range. Specifically, the wide working temperature window (from 50 K to 295 K) of $\text{Gd}_{85}\text{Co}_5\text{Al}_{10}$ is critical for its application in refrigerators. This makes refrigeration applicable at both room temperature and liquid nitrogen temperature.

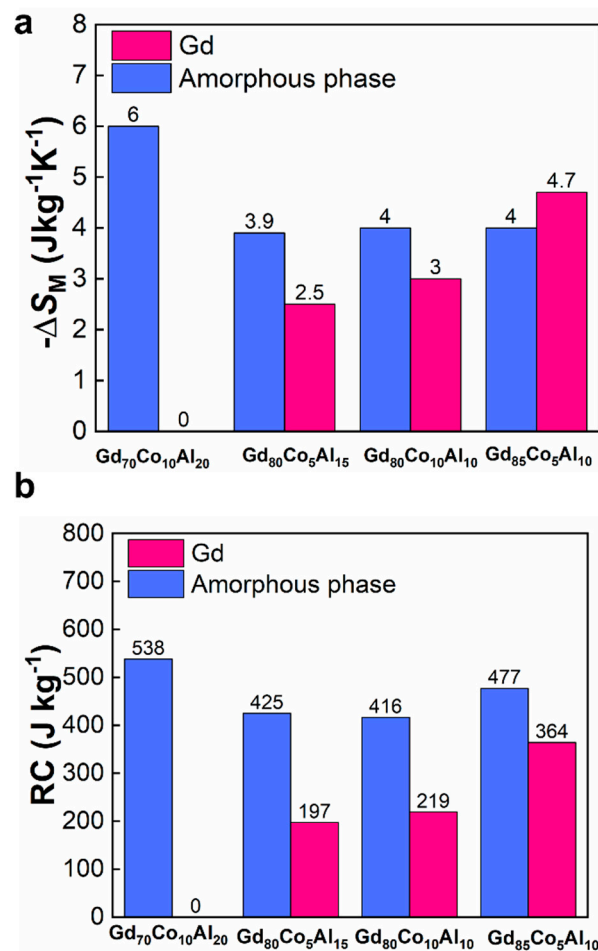


Figure 8. (a) $-\Delta S_M$ and (b) RC for Gd-Co-Al fibers contributed by amorphous and crystalline phases, respectively.

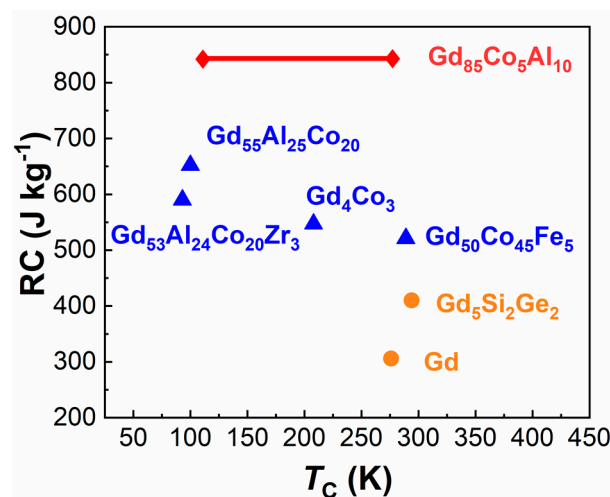


Figure 9. The RC and T_C of different Gd-based magnetic refrigeration materials, including metal glass (triangular), crystal (circular), and Gd₈₅Co₅Al₁₀ (rhombus) listed in Table 1.

4. Conclusions

By adjusting the Gd content, the transition of Gd-Co-Al magnetic refrigeration material from amorphous fiber to ANCF was realized. We found that the RC of Gd₈₅Co₅Al₁₀ reaches 841 J kg⁻¹ and the temperature range extended from 50 K to 295 K, which contributed to excellent MCE. This result suggests that the amorphous/crystalline composite, produced by

controlling the Gd content, is a superior method to obtain a promising magnetic refrigerant from room temperature to liquid nitrogen temperature, which is not only for achieving giant RC but also for obtaining a wide temperature range.

Author Contributions: Data curation, F.C. and K.H.; Formal analysis, F.C., K.H., M.G., Y.Z., W.X., J.H., C.Z., L.S. and J.-Q.W.; Funding acquisition, J.H.; Investigation, F.C., K.H., M.G., Y.Z., W.X., J.H., C.Z., L.S. and J.-Q.W.; Methodology, F.C., J.H., C.Z., L.S. and J.-Q.W.; Writing—original draft, F.C., K.H., M.G., Y.Z., J.H., C.Z., L.S. and J.-Q.W. All authors have read and agreed to the published version of the manuscript.

Funding: This research was funded by the National Natural Science Foundation of China (NSFC 51827801), Youth Innovation Promotion Association CAS (No. 2019296), Zhejiang Provincial Natural Science Foundation of China (LR22E010004).

Data Availability Statement: Not applicable.

Conflicts of Interest: The authors declare no conflict of interest.

References

1. Guillou, F.; Pathak, A.K.; Paudyal, D.; Mudryk, Y.; Wilhelm, F.; Rogalev, A.; Pecharsky, V.K. Non-hysteretic first-order phase transition with large latent heat and giant low-field magnetocaloric effect. *Nat. Commun.* **2018**, *9*, 2925. [[CrossRef](#)] [[PubMed](#)]
2. Kimmel, A.V.; Kirilyuk, A.; Tsvetkov, A.; Pisarev, R.V.; Rasing, T. Laser-induced ultrafast spin reorientation in the antiferromagnet TmFeO₃. *Nature* **2004**, *429*, 850–853. [[CrossRef](#)] [[PubMed](#)]
3. Yuan, Y.; Wu, Y.; Tong, X.; Zhang, H.; Wang, H.; Liu, X.J.; Ma, L.; Suo, H.L.; Lu, Z.P. Rare-earth high-entropy alloys with giant magnetocaloric effect. *Acta Mater.* **2017**, *125*, 481–489. [[CrossRef](#)]
4. Fukamichi, K.; Fujita, A.; Fujieda, S. Large magnetocaloric effects and thermal transport properties of La(FeSi)₍₁₃₎ and their hydrides. *J. Alloys Compd.* **2006**, *408*, 307–312. [[CrossRef](#)]
5. Huo, J.T.; Wang, J.Q.; Wang, W.H. Denary high entropy metallic glass with large magnetocaloric effect. *J. Alloys Compd.* **2019**, *776*, 202–206. [[CrossRef](#)]
6. Feng, J.Q.; Liu, Y.H.; Sui, J.H.; He, A.N.; Xia, W.X.; Wang, W.H.; Wang, J.Q.; Huo, J.T. Giant refrigerant capacity in Gd-based amorphous/nanocrystalline composite fibers. *Mater. Today Phys.* **2021**, *21*, 100528. [[CrossRef](#)]
7. Feng, J.Q.; Li, F.M.; Wang, G.; Wang, J.Q.; Huo, J.T. Magnetocaloric effect in ercu-based metallic glass composite. *J. Non Cryst. Solids* **2020**, *536*, 120004. [[CrossRef](#)]
8. Franco, V.; Borrego, J.M.; Conde, C.F.; Conde, A.; Stoica, M.; Roth, S. Refrigerant capacity of FeCrMoCuGaPCB amorphous alloys. *J. Appl. Phys.* **2006**, *100*, 083903. [[CrossRef](#)]
9. Franco, V.; Conde, A. Scaling laws for the magnetocaloric effect in second order phase transitions: From physics to applications for the characterization of materials. *Int. J. Refrig.* **2010**, *33*, 465–473. [[CrossRef](#)]
10. Huo, J.T.; Zhao, D.Q.; Bai, H.Y.; Axinte, E.; Wang, W.H. Giant magnetocaloric effect in Tm-based bulk metallic glasses. *J. Non Cryst. Solids* **2013**, *359*, 1–4. [[CrossRef](#)]
11. Li, F.M.; Feng, J.Q.; Yi, J.; Wang, G.; Wang, J.Q.; Huo, J.T. Magnetocaloric properties of LaFe_{11.4}Si_{1.6} based amorphous alloys. *J. Alloys Compd.* **2020**, *845*, 156191. [[CrossRef](#)]
12. Liu, G.L.; Zhao, D.Q.; Bai, H.Y.; Wang, W.H.; Pan, M.X. Room temperature table-like magnetocaloric effect in amorphous Gd₅₀Co₄₅Fe₅ ribbon. *J. Phys. D Appl. Phys.* **2016**, *49*, 055004. [[CrossRef](#)]
13. Luo, Q.; Zhao, D.Q.; Pan, M.X.; Wang, W.H. Magnetocaloric effect in Gd-based bulk metallic glasses. *Appl. Phys. Lett.* **2006**, *89*, 081914. [[CrossRef](#)]
14. Shao, Y.Z.; Zhang, J.X.; Lai, J.K.L.; Shek, C.H. Magnetic entropy in nanocomposite binary gadolinium alloys. *J. Appl. Phys.* **1996**, *80*, 76–80. [[CrossRef](#)]
15. Shen, H.X.; Wang, H.; Liu, J.S.; Xing, D.W.; Qin, F.X.; Cao, F.Y.; Chen, D.M.; Liu, Y.F.; Sun, J.F. Enhanced magnetocaloric and mechanical properties of melt-extracted Gd₅₅Al₂₅Co₂₀ micro-fibers. *J. Alloys Compd.* **2014**, *603*, 167–171. [[CrossRef](#)]
16. Tang, B.Z.; Guo, D.Q.; Xia, L.; Ding, D.; Chan, K.C. Magnetoelastic and magnetocaloric properties of Tb_{62.5}Co_{37.5} amorphous alloy. *J. Alloys Compd.* **2017**, *728*, 747–751. [[CrossRef](#)]
17. Yu, P.; Zhang, J.Z.; Xia, L. Fe₈₇Zr₇B₄Co₂ amorphous alloy with excellent magneto-caloric effect near room temperature. *Intermetallics* **2018**, *95*, 85–88. [[CrossRef](#)]
18. Yuan, F.; Du, J.; Shen, B.L. Controllable spin-glass behavior and large magnetocaloric effect in Gd-Ni-Al bulk metallic glasses. *Appl. Phys. Lett.* **2012**, *101*, 032405. [[CrossRef](#)]
19. Zheng, Z.G.; Zhong, X.C.; Liu, Z.W.; Zeng, D.C.; Franco, V.; Zhang, J.L. Magnetocaloric effect and critical behavior of amorphous (Gd₄Co₃)_{1-x}Si_x alloys. *J. Magn. Magn. Mater.* **2013**, *343*, 184–188. [[CrossRef](#)]
20. Luo, Q.; Wang, W.H. Magnetocaloric effect in rare earth-based bulk metallic glasses. *J. Alloys Compd.* **2010**, *495*, 209–216. [[CrossRef](#)]
21. Zheng, Q.; Zhang, L.; Du, J. Table-like magnetocaloric effect in Gd-Ni-Al amorphous/nanocrystalline composites. *J. Phys. D Appl. Phys.* **2017**, *50*, 355601. [[CrossRef](#)]

22. Fu, H.; Zou, M. Magnetic and magnetocaloric properties of ternary Gd–Co–Al bulk metallic glasses. *J. Alloys Compd.* **2011**, *509*, 4613–4616. [[CrossRef](#)]
23. Shao, L.; Xue, L.; Luo, Q.; Wang, Q.; Shen, B. The role of Co/Al ratio in glass-forming GdCoAl magnetocaloric metallic glasses. *Materialia* **2019**, *7*, 100419. [[CrossRef](#)]
24. Bao, Y.; Shen, H.X.; Huang, Y.J.; Xing, D.W.; Wang, H.; Liu, J.S.; Li, H.C.; Yin, H.B.C.; Jiang, S.D.; Sun, J.F.; et al. Table-like magnetocaloric behavior and enhanced cooling efficiency of a Bi-constituent Gd alloy wire-based composite. *J. Alloys Compd.* **2018**, *764*, 789–793. [[CrossRef](#)]
25. Zhong, X.C.; Shen, X.Y.; Mo, H.Y.; Jiao, D.L.; Liu, Z.W.; Qiu, W.Q.; Zhang, H.; Ramanujan, R.V. Table-like magnetocaloric effect and large refrigerant capacity in Gd₆₅Mn₂₅Si₁₀-Gd composite materials for near room temperature refrigeration. *Mater. Today Commun.* **2018**, *14*, 22–26. [[CrossRef](#)]
26. Zheng, Q.; Zhang, L.L.; Du, J. Magnetic entropy change in Gd₉₅Fe_{2.8}Al_{2.2} amorphous/nanocrystalline ribbons. *Scr. Mater.* **2017**, *130*, 170–173. [[CrossRef](#)]
27. Shen, H.X.; Wang, H.; Liu, J.S.; Cao, F.Y.; Qin, F.X.; Xing, D.W.; Chen, D.M.; Liu, Y.F.; Sun, J.F. Enhanced magnetocaloric properties of melt-extracted GdAlCo metallic glass microwires. *J. Magn. Magn. Mater.* **2014**, *372*, 23–26. [[CrossRef](#)]
28. Sheng, W.; Wang, J.Q.; Wang, G.; Huo, J.T.; Wang, X.M.; Li, R.W. Amorphous microwires of high entropy alloys with large magnetocaloric effect. *Intermetallics* **2018**, *96*, 79–83. [[CrossRef](#)]
29. Jiang, S.D.; Wang, H.; Huang, Y.J.; Shen, H.X.; Xing, D.W.; Ning, Z.L.; Sun, J.F. Effect of strain rate on tensile behavior in amorphous fibers by an in-situ video extensometer system. *Mater. Sci. Eng. A* **2020**, *782*, 139252. [[CrossRef](#)]
30. Sherrington, D.; Kirkpatrick, S. Solvable model of a spin-glass. *Phys. Rev. Lett.* **1975**, *35*, 1792–1796. [[CrossRef](#)]
31. Zhang, J.L.; Zheng, Z.G.; Cao, W.H.; Shek, C.H. Magnetic behavior of Gd₄Co₃ metallic glass. *J. Magn. Magn. Mater.* **2013**, *326*, 157–161. [[CrossRef](#)]
32. Gschneidner, K.A., Jr.; Pecharsky, V.K.; Tsokol, A.O. Recent developments in magnetocaloric materials. *Rep. Prog. Phys.* **2005**, *68*, 1479–1539. [[CrossRef](#)]
33. Pecharsky, V.K.; Gschneidner, K.A., Jr. Magnetocaloric effect and magnetic refrigeration. *J. Magn. Magn. Mater.* **1999**, *200*, 44–56. [[CrossRef](#)]
34. Yan, J.; Shi, K.W.; Deng, S.H.; Zhao, W.J.; Lu, H.Q.; Sun, Y.; Chen, Y.L.; Wang, C. The influence of combination of the first-order and second-order phase transitions on magnetocaloric effects in Mn₃Cu_{1-x}Fe_xN. *Solid State Commun.* **2018**, *282*, 33–37. [[CrossRef](#)]
35. Fan, J.; Ling, L.; Hong, B.; Zhang, L.; Pi, L.; Zhang, Y. Critical properties of the perovskite manganite La_{0.1}Nd_{0.6}Sr_{0.3}MnO₃. *Phys. Rev. B* **2010**, *81*, 144426. [[CrossRef](#)]
36. Guo, D.; Moreno-Ramírez, L.M.; Romero-Muñoz, C.; Zhang, Y.; Law, J.-Y.; Franco, V.; Wang, J.; Ren, Z. First- and second-order phase transitions in RE₆Co₂Ga (RE = Ho, Dy or Gd) cryogenic magnetocaloric materials. *Sci. China Mater.* **2021**, *64*, 2846–2857. [[CrossRef](#)]
37. Huo, J.T.; Huo, L.S.; Li, J.W.; Men, H.; Wang, X.M.; Inoue, A.; Chang, C.T.; Wang, J.Q.; Li, R.W. High-entropy bulk metallic glasses as promising magnetic refrigerants. *J. Appl. Phys.* **2015**, *117*, 073902. [[CrossRef](#)]
38. Atalay, S.; Gencer, H.; Kolat, V.S. Magnetic entropy change in Fe_{74-x}Cr_xCu₁Nb₃Si₁₃B₉ (x = 14 and 17) amorphous alloys. *J. Non Cryst. Solids* **2005**, *351*, 2373–2377. [[CrossRef](#)]
39. Franco, V.; Blazquez, J.S.; Conde, A. The influence of Co addition on the magnetocaloric effect of Nanoperm-type amorphous alloys. *J. Appl. Phys.* **2006**, *100*, 064307. [[CrossRef](#)]
40. Kim, K.S.; Min, S.G.; Yu, S.C.; Oh, S.K.; Kim, Y.C.; Kim, K.Y. The large magnetocaloric effect in amorphous Fe_{91-x}Y_xZr₉ (x = 0, 5, 10) alloys. *J. Magn. Magn. Mater.* **2006**, *304*, e642–e644. [[CrossRef](#)]
41. Kolano-Burian, A.; Kowalczyk, M.; Kolano, R.; Szymczak, R.; Szymczak, H.; Polak, M. Magnetocaloric effect in Fe–Cr–Cu–Nb–Si–B amorphous materials. *J. Alloys Compd.* **2009**, *479*, 71–73. [[CrossRef](#)]
42. Min, S.G.; Kim, K.S.; Yu, S.C.; Suh, H.S.; Lee, S.W. Analysis of magnetization and magnetocaloric effect in amorphous FeZrMn ribbons. *J. Appl. Phys.* **2005**, *97*, 10M310. [[CrossRef](#)]